Promoting electrocatalytic CO_2 reduction on nitrogen-doped carbon with sulfur addition

Fuping Pan[a], Boyang Li[b], Wei Deng[a], Zichen Du[a], Yang Gang[a], Guofeng Wang[b],*, Ying Li[a],*

[a] J. Mike Walker '66 Department of Mechanical Engineering, Texas A&M University, College Station, TX 77843, United States
[b] Department of Mechanical Engineering and Materials Science, University of Pittsburgh, Pittsburgh, PA 15261, United States

ARTICLE INFO

ABSTRACT

Electrochemical reduction of CO_2 on metal-free N-doped carbon (N-C) catalysts offers an emerging route to transform CO_2 into value-added fuels. However, it suffers poor efficiency when operated at low overpotentials. Herein, we demonstrated that sulfur (S) addition could greatly enhance catalytic CO_2 reduction activity and selectivity of N-C. The N,S-codoped carbon catalysts exhibited a high CO Faradaic efficiency of 92% and a CO current of $2.63\,\mathrm{mA\,cm^{-2}}$ at a low overpotential of 490 mV, much better than that of the S-free N-C counterpart. By correlating dopant configurations with catalytic performance of model catalysts and combining theoretical density functional theory (DFT) calculations, we revealed that incorporating S in N-C leads to the generation of a higher density of pyridinic N that serves as the determining active site for CO_2 activation. In addition, S dopants significantly promote the catalytic reactivity and selectivity of pyridinic and graphitic N by decreasing the free energy barrier for key intermediate *COOH formation. The experimental findings and theoretical understanding of the dual-doping promotion effects reported in this work have provided insights on designing high-performance carbon catalysts for CO_2 conversion.

1. Introduction

Electrochemical reduction of CO_2 offers an environmentally benign and sustainable route to mitigate atmospheric CO_2 concentrations and generate value-added fuels and feedstock simultaneously [1,2]. Among a variety of reaction routes and products, the reduction of CO_2 to CO $(CO_2 + 2H^+ + 2e^- \rightarrow CO + H_2O, -0.11\,\mathrm{V}$ versus RHE) is reported to be more economically viable in practice due to less energy input required and relatively high selectivity [3,4]. However, the current electrocatalytic CO_2-to-CO process imposes great technological challenges owing to the inherently sluggish kinetics of CO_2 reduction reaction (CO_2RR) and inevitable competition with hydrogen evolution reaction (HER) in aqueous media [5–7]. Noble metals such as Au and Ag are the state-of-the-art catalysts that can selectively reduce CO_2 to CO while effectively suppressing HER [8,9]; however, they suffer from high cost and limited availability. Developing non-precious, selective, and stable CO_2RR electrocatalysts is thus highly demanded.

Recent studies have demonstrated that metal-free nitrogen-doped carbon (N-C) materials showed appealing catalytic performance for CO_2 reduction to CO [5,10–12], representing a new generation of promising alternatives to noble metals due to low cost and sustainable availability. Based on theoretical calculation and experimental investigation, the catalytic CO_2RR nature of N-C was found to originate from the electronic modulation of conjugated sp^2 C atoms with adjacent N dopants, which breaks electroneutrality through delocalizing π-orbital electrons in the carbon frameworks, thus creating active sites for CO_2 activation [5,11,13]. In addition, the weak interaction between N-C and CO results in the facile desorption of CO from the N-C surface and thus permits high CO selectivity without being further transformed into hydrocarbons [13]. Consequently, N doped graphene [13], carbon nanotube [14], and porous carbon [15] have been fabricated and studied for CO_2RR. Nevertheless, most of them either required excessive overpotentials to reach acceptable Faradaic efficiency or exhibited poor CO currents at low overpotentials [14,16–20]. It is therefore highly imperative to develop a new strategy to improve the catalytic performance of N-C materials for achieving highly efficient CO_2-to-CO conversion.

Because catalytic CO_2RR sites on N-C are derived from N atoms modification, the intrinsically catalytic nature of N-C thus depends strongly on the configurations of N dopants and their local electronic properties [5,13,14]. However, the efforts in exploring catalytically active N sites and understanding reaction mechanisms are still insufficient [5,13,14,21]. There are debates on whether the most active sites are created by pyridinic N or graphitic N. Regarding the electronic properties of N dopants that affect the inherent catalytic capability,

* Corresponding authors.
E-mail addresses: guw8@pitt.edu (G. Wang), yingli@tamu.edu (Y. Li).

previous studies showed that they can be engineered through modulating nearby carbon compositions [22,23]. Researchers have proposed to employ a chemical dual-doping approach to tune local electronic environment of N-C by incorporating secondary heteroatoms for various electrocatalysis, and the observed activity enhancement of the co-doped catalysts was generally believed to be derived from synergistic effects between N and secondary atoms [22,24–28]. For instance, Dai et al. [24] and Chen et al. [29] reported N,S dual-doped graphene for catalyzing oxygen reduction reaction, which showed significantly better activity than the counterparts doped solely with N. The computational simulation predicted that incorporating S into N-doped graphene could increase asymmetrical spin density of C system owing to greater polarizability of S atoms compared to N and C atoms [5,24,30,31], giving rise to enhanced performance. Regarding CO_2 electroreduction, the transfer of the electron from active centers to the antibonding orbitals of CO_2 molecules is considered to be the most critical step in the CO_2 activation process [32]. It was also proposed that carbon structures with enhanced spin density are beneficial for CO_2 activation because of the accelerated electron transfer and improved binding interaction with CO_2RR-involved intermediates [30,33].

In view of abovementioned understanding, we hypothesized that S modification could be a potentially effective route to boost CO_2RR performance over N-C materials derived from S-donated electronic contribution. However, to the best of our knowledge, implementation of S decoration strategy has rarely been reported for electrocatalytic CO_2 reduction. Here, we explored the use of S incorporation to promote CO_2 electroreduction to CO over N-C by combining experimental investigation and theoretical density functional theory (DFT) calculations. Experimentally, N-C layers and N,S-codoped carbon layers (NS-C) with similar carbon architecture and tunable N,S contents/configurations were synthesized via a facile layer-structured carbon nitride-templated pyrolysis strategy. These carbon layer materials were further applied as model catalysts to evaluate their catalytic CO_2RR behaviors. Theoretically, the Gibbs free energy for the formation of *COOH intermediate on various N-doped and N,S-codoped moieties were calculated to unravel active sites and S-modulated roles on catalytic CO_2RR mechanisms and nature of N dopants. The energy for the competitive HER was also calculated in order to elucidate the CO selectivity on the NS-C catalyst. The potential contribution of S modulation in decreasing overpotentials and increasing selectivity/current for CO production over N-C was systematically evaluated.

2. Experimental

2.1. Synthesis of catalysts

In a typical synthesis of NS-C, 0.3 g of citric acid and 10 g of thiourea were added in 50 mL of deionized water. The mixture was then heated at 80 °C with stirring in an open system to evaporate the water. Subsequently, the dried solids were ground into fine powders, which were then calcined in a tube furnace under Ar atmosphere at 550 °C for 2 h and further raised to final temperatures of 800, 900, and 1000 °C for 1 h, and as-prepared catalysts were denoted as NS-C-800, NS-C-900, and NS-C-1000, respectively. For comparison, S-free N-C-900 was also prepared using the same method as to NS-C-900 except replacing thiourea with urea.

2.2. Electrochemical CO_2RR activity measurements

Electrocatalytic CO_2RR activity was evaluated in a two-compartment H-type electrochemical cell using a standard three-electrode configuration in CO_2-saturated 0.1 M $KHCO_3$ electrolyte (pH = 6.8). A Pt foil and an Ag/AgCl (filled with 3 M KCl) were used as the counter electrode and reference electrode, respectively. The measured potentials after iR compensation were rescaled to the reversible hydrogen electrode by E (RHE) = E (Ag/AgCl) + 0.210 V + 0.0591V × pH. The

working electrode was prepared by drop casting catalyst ink onto a carbon paper (1 cm^2) with a mass loading of 0.8 mg cm^{-2}. The ink was prepared by dispersing 3 mg catalysts in a mixture solution of 200 μL DI-water, 370 μL ethanol, and 30 μL 5% Nafion solution via sonication for 3 h. The counter electrode was placed in the anode chamber, while the working and reference electrodes were placed in the cathode chamber, which was separated by a piece of Nafion 115 ionic exchange membrane (Fuel cell store) to avoid the re-oxidation of CO_2RR-generated products. High-purity CO_2 was introduced in the cathode chamber for 1 h with a flow rate of 34 mL min^{-1} to saturate the electrolyte before starting electrolysis and maintained this flow rate during measurements. The catholyte was stirred at 900 rpm during all tests. The gas-phase products were analyzed via an online gas chromatograph (GC, Fuel Cell GC-2014ATF, Shimadzu) equipped with a thermal conductivity detector (TCD) and a methanizer assisted flame ionization detector (FID). The liquid-products were characterized by a nuclear magnetic resonance (NMR) spectrometer (Bruker avance III 500 MHz), and no liquid products were detected.

Faradaic efficiency (FE) of gaseous products at each applied potential was calculated based on the equation:

$$FE = \frac{z \cdot P \cdot F \cdot V \cdot v_i}{R \cdot T \cdot J}$$

where z is the number of electrons transferred per mole of gas product (z is 2 for CO and H_2), F is Faraday constant (96,500 C mol^{-1}), P is the pressure (1.01 × 10^5 Pa), V is the gas volumetric flow rate (5.67 × 10^{-7} $m^3 s^{-1}$), v_i is the volume concentration of gas product determined by GC, T is the temperature (298.15 K), R is the gas constant (8.314 J $mol^{-1} K^{-1}$), and J is the steady-state current at each applied potential (A).

2.3. Density functional theory (DFT) calculations

Structure optimization and electronic energy calculations were performed using the first principles spin-polarized DFT method as implemented in the Vienna ab initio simulation package (VASP) code. Projector augmented wave (PAW) pseudopotential was employed to describe the core electrons. The cutoff energy was set as 400 eV to expand the wave functions. Electronic exchange and correction were described by generalized gradient approximation (GGA) of the revised Perdew, Burke and Ernzernhof (RPBE) functionals. Various N-doped and N, S co-doped graphene (such as hole, edge, and bulk) models were constructed as the active sites for CO_2RR. The Brillouin Zone was sampled by 3 × 1 × 1, 1 × 3 × 1, and 6 × 5 × 1 Monkhorst-pack k-point meshes for the hole, edge and bulk active site models, respectively. For each structure, the atomic positions were optimized until the force fell below 0.01 eV/Å.

The computational hydrogen electrode (CHE) was used to calculate the free energy of each intermediate state [34]. The free energy of a chemical reaction is calculated by

$$\Delta G = \Delta E_{DFT} + \Delta E_{ZPE} + \Delta E_{solv} + \Delta H_{0 \, to \, T} - T \Delta S$$

where ΔE_{DFT} is the energy change calculated by DFT method, ΔE_{ZPE} is the zero-point energy correction, ΔE_{solv} is the solvation energy correction, $\Delta H_{0 \, to \, T}$ is the reaction enthalpy change from 0 to T K, and ΔS is the reaction entropy change. The solvation effect correction was 0.25 eV stabilization of COOH*, 0.1 eV stabilization of CO*. ZPE corrections were calculated as $ZPE = \sum (1/2)h v_i$, where h is Planck's constant and v_i is the frequency of the corresponding vibrational mode of binding molecules. $\Delta H_{0 \, to \, T}$ was calculated by the vibrational heat capacity integration $\int_0^t C_p dT$. The entropy terms for gas phase were derived from partition functions and compared with the data from NIST Standard reference database.
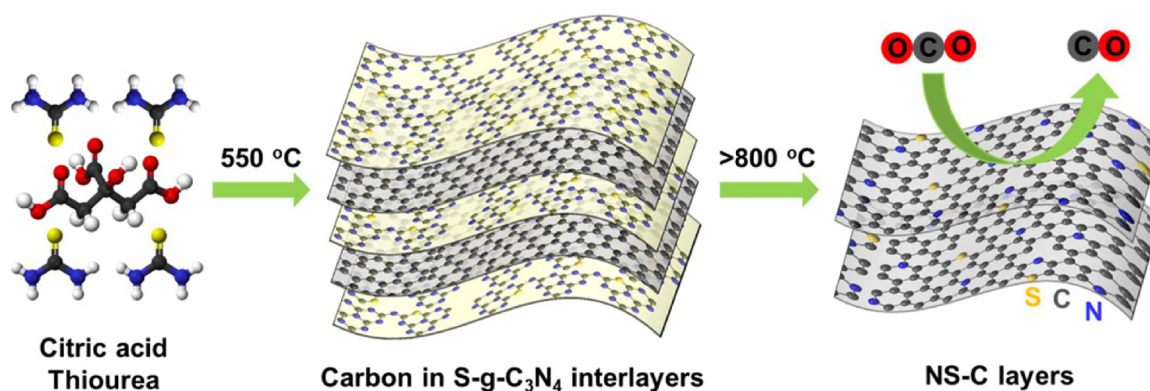
Fig. 1. Schematic illustration showing the synthesis processes of NS-C layers.

3. Results and discussion

The synthesis of NS-C layers involves a facile solid-state pyrolysis procedure using thiourea as N,S source and citric acid as C source, as schematically depicted in Fig. 1. Thermal condensation of thiourea at 550 °C can create layer-structured graphitic S-doped carbon nitride (g-S-C$_3$N$_4$) (Fig. S1) [35,36], which functions as a templated reactor to bond citric acid-derived aromatic carbon intermediates into the interlayer of g-S-C$_3$N$_4$. The space-confined effect thus directs the evolution of two-dimensional (2D) carbon nanosheets structure. When heating temperature goes above 800 °C, the complete thermolysis of g-S-C$_3$N$_4$ generates the carbon layers due to the low thermostability of g-S-C$_3$N$_4$ templates [37,38]. During the overall annealing process, the released abundant N,S-containing gases act as N,S feedstock for incorporating N,S atoms into the carbon lattices by directly substituting C atoms and/or reacting with oxygen groups attached on carbon intermediates [38–40]. The doped N,S contents can be readily tuned by adjusting annealing temperatures; the samples prepared at 800, 900, and 1000 °C were denoted as NS-C-800, NS-C-900, and NS-C-1000, respectively. In order to explore effects of S modification on the catalytic CO$_2$RR activity of N-C, S-free N-C layer was also prepared using the same synthesis procedure as that of NS-C-900 except replacing thiourea with urea (named as N-C-900). The similar molecular structure and polymerization/decomposition process between urea and thiourea ensure analogous layer nanostructure of N-C and NS-C [41], providing ideal catalysts to investigate the effects of N,S dual-doping on catalytic origin toward CO$_2$ reduction.

To illustrate the microscopic morphology of NS-C catalysts, transmission electron microscopy (TEM) and scanning electron microscopy (SEM) imaging were performed. As revealed by a TEM image in Fig. 2a, NS-C-900 exhibited a crumpled flake-like morphology, which is also confirmed by scanning TEM (Fig. 2c) and SEM (Fig. S2) observation. The SEM image also shows the presence of meso/macropores. A high-resolution TEM image (Fig. 2b) clearly shows distorted short-range graphitic stripes with a thickness of about 5 nm, suggesting the formation of multi-layer graphene domains. The interlayer distance was estimated to be about 0.35 nm, in consistent with a typical graphitic structure. In addition, it is apparent that NS-C-900 showed wrinkles, interlaces, and fractures, which may be attributed to the local stress created by lattice defects (e.g. N,S dopants, vacancies) and to the etching effects induced by numerous NH$_3$ gases generated during the decomposition of thiourea and g-S-C$_3$N$_4$ [42–44]. The successful doping of N and S is verified by elemental mapping images (Fig. 2c), which display the homogeneous distribution of N and S species in the carbon frameworks. To verify that the ultra-thin layer characteristic of NS-C stems from the duplication of layer-structured g-S-C$_3$N$_4$ (Fig. 1), a controlled experiment by directly carbonizing citric acid at 900 °C was carried out. As depicted in Fig. S3, the obtained sample showed a thick plate-like feature instead of a thin layer, directly manifesting the crucial

templated role of g-S-C$_3$N$_4$ in navigating the generation of graphene-like architecture. Similarly, N-C-900 possessed the entangled layer morphology (Fig. S4), which is analogous to that of NS-C-900 due to the similar synthetic procedure (Fig. S5).

X-ray diffraction (XRD) and Raman spectroscopy were conducted to investigate the crystalline structure of N-C and NS-C samples. As shown in Fig. 2d, all samples exhibited broad diffraction patterns characteristic, indicative of an amorphous nature due to the low carbonization temperature; the two peaks at around 25.8° and 41° correspond to (0 0 2) and (1 0 0) planes of the carbon, respectively. On the other hand, Raman spectra (Fig. 2e) of all samples show two vibrational bands centered at 1342 cm^{-1} (D band) and 1590 cm^{-1} (G band). The D band and G band are associated with the defects and the bond stretching of the sp^2 carbon, respectively [45]; a higher I$_D$/I$_G$ ratio reflects more defective carbon structure. The I$_D$/I$_G$ ratios for N-C-900, NS-C-800, NS-C-900 and NS-C-1000 were calculated to be 1.11, 1.28, 1.20, and 1.17, respectively. It is thus inferred that more defects were generated in N-C upon S doping, probably due to the larger radius of S atoms relative to N and C atoms that breaks the integrity of hexagonal carbon structure. Moreover, it can be seen that the I$_D$/I$_G$ values of NS-C decrease with increasing of the annealing temperature, which can be attributed to the loss of N,S atoms at elevated temperatures.

The surface area and pore structure of the resultant catalysts were determined by N$_2$ adsorption/desorption measurements. As depicted in Fig. 3a, all curves show sharp uptake at a relatively high-pressure range more than 0.45 accompanied with the hysteresis loops, indicating the presence of dominant mesopores, which can be further verified by the pore size distributions (Fig. 3b). The Brunauer–Emmett–Teller (BET) surface areas of N-C-900, NS-C-800, NS-C-900, and NS-C-1000 were calculated to be 126, 90, 160, and 119 m^2 g^{-1}, respectively; and the pore volumes being 0.2, 0.17, 0.28, and 0.22 cm^3 g^{-1} (Table S1), respectively. These results demonstrate that the use of thiourea contributes to increasing the surface area and pore volume as compared to urea. In addition, it is shown that the heating temperature plays a key role in determining the surface area and pore volume, both of which increased from 800 to 900 °C and then decreased at 1000 °C. This may be because that heating at a higher temperature of 900 °C leads to the more complete decomposition of the g-S-C$_3$N$_4$ polymer templates, resulting in a larger porosity achieved on NS-C-900 than that of NS-C-800 (Fig. 3b). However, overheating at 1000 °C may cause the collapse of mesoporous architecture of carbon layer frameworks, which potentially decreases the surface area and pore volume, as evidenced by the pore distributions (Fig. 3b).

Surface compositions were determined by X-ray photoelectron spectroscopy (XPS). The XPS spectra reveal the presence of N 1s at 400 eV and S 2p at 170 eV (Fig. 4). In contrast, N-C-900 exhibited an S-free survey spectrum (Fig. 4a), indicating the successful incorporation of S atoms in N-C. The N contents were calculated to be 12.59, 20.02, 13.80, and 7.22 at.%, and S contents are 0, 1.04, 0.85, and 0.79 at.% for
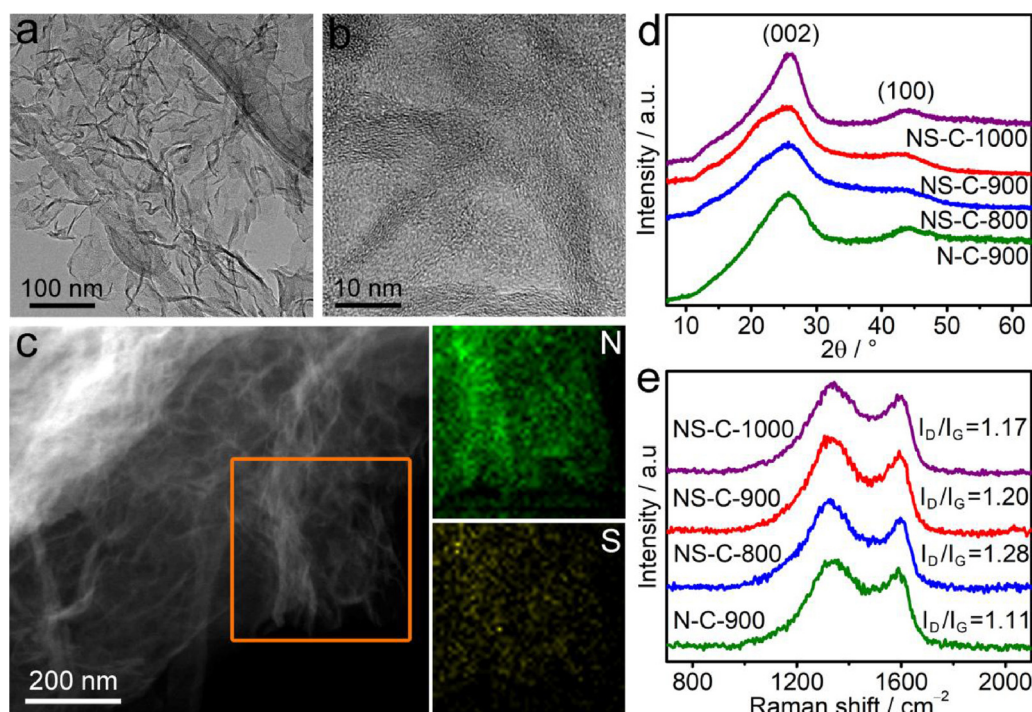
Fig. 2. (a) TEM, (b) high-resolution TEM, (c) scanning TEM and N,S elemental mapping images of NS-C-900. (d) XRD patterns and (e) Raman spectra of N-C-900 and NS-C.
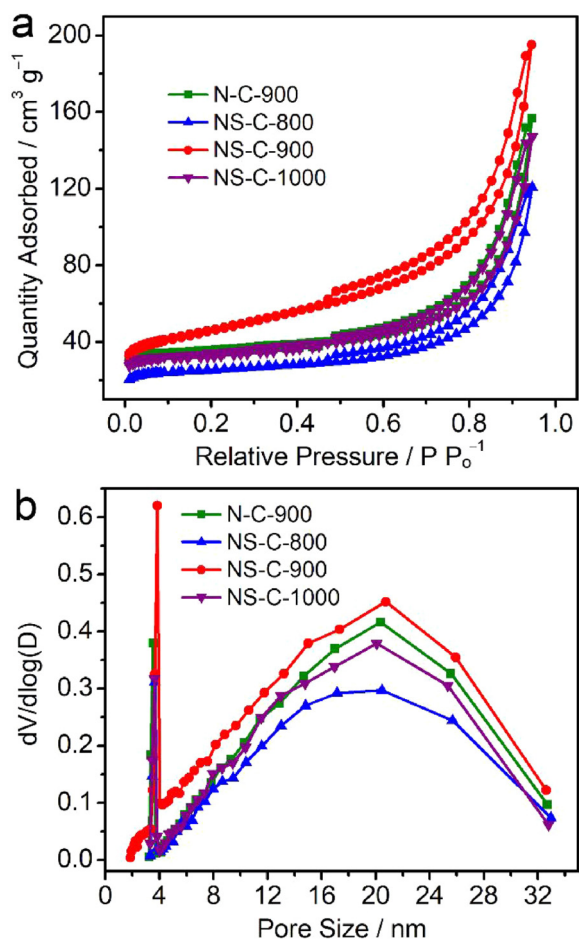
Fig. 3. (a) N$_2$ adsorption/desorption isotherms and (b) pore size distributions of N-C-900 and NS-C.

N-C-900, NS-C-800, NS-C-900, and NS-C-1000 (Table S1), respectively. Note that the N,S concentrations decrease when increasing the pyrolysis temperature, which is probably as a consequence of the thermolysis of unstable N,S-containing functionalities at a high-temperature heating process. Furthermore, it was observed that S contents are significantly lower than N contents in all NS-C samples. It appears that this result agrees with those from the literature that most of reported S,N-doped carbons had low S contents ranging from 0.2 to 1.5 at.% within heating temperatures of 800–1000 °C [24,27,29,38,39,46–49]. This may be because that the S atom has a rather larger radius than the C,N atoms, which makes that the S atom is more difficult to be incorporated into the carbon lattices, resulting in a kinetically slow doping process of S as compared to N. Noted that, although N,S-codoped carbons have relatively low S contents, the significant contribution from S atoms toward electrocatalytic reactions are unequivocal and have been widely demonstrated for oxygen reduction reaction [24,27,29,38,39,46–49].

We further analyzed high-resolution XPS spectra of S and N to determine the bonding configurations of the dopants. The S 2p spectra (Fig. 4a) at lower binding energy can be assigned to C−S−C (2p$_{3/2}$ at 164.1 and 2p$_{1/2}$ at 165.3 eV), and the peaks centered at 167.6 and 168.8 eV correspond to oxidized species (C−SOx−C) [39,50]. In NS-C-800, the percentages of C−S−C and C−SOx−C species are almost equal (48% vs. 52%) (Fig. 4c), while C−S−C becomes dominant at more than 70% for samples prepared at an annealing temperature above 900 °C. This observation suggests that the oxidized S group was gradually converted into C−S−C at the high-temperature carbonization process [23]. As for N 1s spectra (Fig. 4b), they can be deconvoluted into three peaks centered at 397.9, 400.5, and 403.1 eV, corresponding to pyridinic N (Pyri-N), graphitic N (Grap-N), and oxidized N (Oxid-N), respectively [44,50–54]. It is worth noting that the Pyri-N percentage gradually decreases from 55% in NS-C-800 to 52% in NS-C-900, and 45% in NS-C-1000 accompanied with the increase in the Grap-N percentage from 39% to 44% and 50% (Fig. 4c), respectively, whereas the Oxid-N percentage remains constant around 5% in all samples. These phenomena signify that Grap-N has a better thermostability than Pyri-N, in consistent with previous reports [52]. On the other hand, compared to N-C-900, NS-C-900 possesses a larger Pyri-N portion (52% vs.
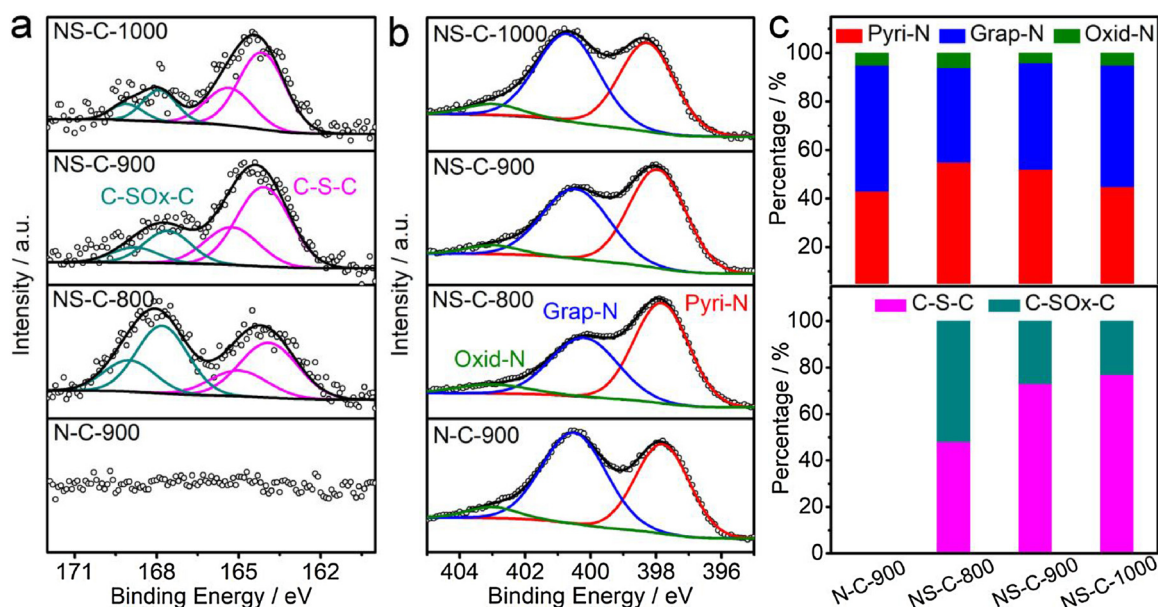
Fig. 4. (a) High-resolution S 2p XPS spectra, (b) high-resolution N 1s XPS spectra, and (c) calculated percentages of N,S species for N-C-900 and NS-C.

43%) but a lower Grap-N percentage (44% vs. 52%), although they were fabricated at the same temperature. The Pyri-N portion of N-C-900 is even lower than that of NS-C-1000 (43% vs. 45%). These results demonstrate that S incorporation helps the formation of Pyri-N while suppressing Grap-N. As reported in the literature [52], Pyri-N is located at the edge of a carbon layer by bonding with two C atoms, and the Grap-N bonding with three neighboring C atoms is completely embedded in the matrix of a carbon layer. In the case of introducing S in N-C, more distorted fractures and defective structure were generated as evidenced by Raman analyses (Fig. 2e), which thus could provide more edge locations to host high-density Pyri-N. Because N dopants are catalytically active sites in the electrocatalytic CO_2RR process, the change in N structures may lead to significant activity variation. In addition, it has been demonstrated that S atoms play pivotal roles in modulating electronic properties of N-C [24], which may also impart NS-C with intriguing catalytic CO_2RR properties.

The electrocatalytic CO_2RR activity was assessed in a two-compartment H-shaped cell using a standard three-electrode configuration with 0.1 M $KHCO_3$ solution as the electrolyte. Linear sweep voltammetry (LSV) was first recorded. As shown in Fig. 5a, the current density of NS-C-900 under the CO_2-saturated solution increases more quickly in comparison with that recorded in the Ar-saturated solution when the applied potential was swept more negatively than -0.3 V, implying the occurrence of CO_2 reduction with hydrogen evolution. In order to determine product selectivity, CO_2 reduction was carried out by constant-potential electrolysis. The reaction gases after electrolysis were vented directly into a gas chromatograph (GC) to quantitatively analyze the gas-phase products, and CO and H_2 were identified as the main products with total Faradaic efficiency (FE) more than 98%. No liquid-phase products were detected by ^1H nuclear magnetic resonance (NMR) spectroscopy. The stable total current densities are shown in Fig. S6, in which NS-C-900 exhibited the largest currents than others at all potential regions. For example, at -0.6 V, NS-C-900 had a total current of $-2.88\,mA\,cm^{-2}$, much larger than that of N-C-900 ($-0.34\,mA\,cm^{-2}$), NS-C-800 ($-0.83\,mA\,cm^{-2}$), and NS-C-1000 ($-1.54\,mA\,cm^{-2}$), respectively. These results show that additional S doping speeds up the CO_2RR rate over N-C and that NS-C prepared at 900 °C possessed the fastest reaction rate among all the samples.

Fig. 5b depicts CO FEs at various potentials. N-C-900 presented an onset CO FE of 13% at -0.40 V, corresponding to an onset overpotential of 290 mV given the equilibrium potential of CO_2/CO is

-0.11 V [14]. The CO FEs increased to the maximum value of 75% at an overpotential of 690 mV and then decreased at more negative potentials. As for NS-C-900, it can be seen that CO generation started at an overpotential of 140 mV with a CO FE of 15%, and the highest CO FE reached 92% at an overpotential of 490 mV. Obviously, compared to N-C-900, NS-C-900 catalyzes CO_2 reduction at a smaller overpotential but with larger CO selectivity, directly suggesting the enhanced inherent reactivity and selectivity for CO_2RR after introducing S into N-C. In addition, it was found that the activity of NS-C depends strongly on the annealing temperature, and 900 °C was the most optimal temperature to yield the highest CO FE (92%) on NS-C-900, which is higher than NS-C-800 (74%) and NS-C-1000 (86%). Accordingly, NS-C-900 exhibited the lowest H_2 FEs than N-C-900 and other NS-C counterparts (Fig. S7), indicating the highest capability in suppressing H_2 evolution on NS-C-900 electrode. Fig. 5c shows the CO partial current density calculated by multiplying CO FEs with the total current density. Among all catalysts, it is notable that NS-C-900 displayed the largest CO currents at all potential ranges, indicating the fastest CO production rate over NS-C-900. For instance, at -0.6 V, the CO current density of NS-C-900 was $-2.63\,mA\,cm^{-2}$, which was about 15, 4, and 2 times as high as that of N-C-900 ($-0.17\,mA\,cm^{-2}$), NS-C-800 ($-0.66\,mA\,cm^{-2}$), and NS-C-1000 ($-1.33\,mA\,cm^{-2}$), respectively. The temperature-dependent CO_2RR performance of NS-C can be ascribed to the variable contents and structures of doped N,S species, thus leading to tunable catalytic behaviors in the CO_2 reduction process. Among the series, the best activity of NS-C-900 can be also partially attributed to its highest surface area and pore volume because they are conducive to expose more active surface and facilitate the mass transport. All these results demonstrate that S addition plays a significant role in improving catalytic capability for the reduction of CO_2 to CO over N-C.

Furthermore, the long-term electrochemical stability of NS-C-900 was investigated via prolonged electrolysis performed at the potential of -0.6 V where the maximum CO FE was achieved. As revealed in Fig. 5d, the current underwent a quick decrease in the first 2 h of electrolysis. After that, the current became almost stable, reaching a stable current of 2 mA cm^{-2} after 20 h continuous operation. As for CO selectivity, NS-C-900 retained stable CO FEs around 91% during the 20 h electrolysis, suggesting good durability of the selective CO_2 reduction to CO. We also characterized the compositions of spent catalyst. We found that the N,S contents decreased from 13.80 to 11.03 at.% for N and from 0.85 to 0.71 at.% for S, while the O content increased from
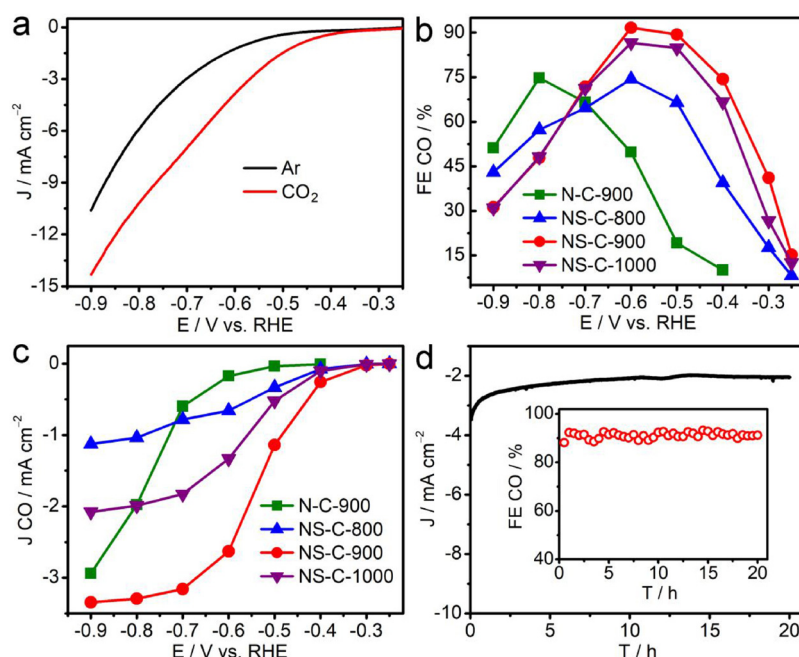
Fig. 5. (a) LSV curves recorded on NS-C-900 in the Ar- and CO_2-saturated 0.1 M $KHCO_3$ solution at a scan rate of 5 mV s^{-1}. (b) CO FEs and (c) CO partial current density of N-C-900 and NS-C. (d) Chronoamperometric responses and CO FEs at -0.6 V on NS-C-900 for stability tests.

4.79 to 7.98 at.%. The loss of N,S dopants might be the reason accounting for the observed current decrease in the beginning of the electrolysis. When compared with metal-free heteroatoms-doped carbon catalysts reported in the literature, the CO_2RR performance of NS-C-900 is comparable to or even outperforming most of them (Table S2). In particular, an overpotential of 490 mV required to reach the highest CO FE of 92% achieved on NS-C-900 is smaller than N-doped porous carbon (820 mV, 78%) [15], g-C_3N_4/carbon nanotube composite (640 mV, 60%) [19], N-doped carbon nanotube (790 mV, 90%) [14], N-doped microporous carbon (550 mV, 40%) [20], fluorine-doped carbon black (510 mV, 91%) [33], and phosphorus-doped onion-like carbon (890 mV, 81%) under similar condition [55]. However, the activity of NS-C-900 is still much lower than those of metal and metal oxide catalysts (Table S3), especially the noble metal-based catalysts. Therefore, further improvement in the CO_2RR activity of metal-free carbons are still highly imperative.

To gain further insights into the reaction kinetics, Tafel plots and electrochemical impedance spectroscopy (EIS) were performed. As shown in Fig. 6a, N-C-900, NS-C-800, NS-C-900, and NS-C-1000 exhibited Tafel slopes of 146, 99, 94, and 102 mV dec^{-1}, respectively. Remarkably, NS-C showed much smaller Tafel slopes than N-C-900, evidencing accelerated reaction kinetics upon S introduction. In addition, all Tafel slops were close to the theoretical value of 118 mV dec^{-1}, indicating that CO_2 reduction proceeds through a mechanism that the initial single electron transfer to form *COOH intermediates is the rate-determining step [33]. The Nyquist plots are depicted in Fig. 6b and the corresponding equivalent circuit model is shown in Fig. S8. In the Nyquist plots, the intercept on the real axis is attributed to solution resistance (R_S). The first semicircle is generally assigned to ohmic resistance (R_Ω), which can be a parameter to present the conductivity of catalysts. The second semicircle corresponds to charge transfer resistance (R_{CT}), which reflects the resistance for electrons to transfer from catalyst surface to the reactants and intermediates [56]. The calculated values of R_S are close for all catalysts due to the same test condition. In addition, it can be seen that NS-C-800 showed the largest R_Ω of 8.8 Ω, suggesting the lowest conductivity. This might be due to the lowest carbonization temperature of 800 °C used to prepare NS-C-800. The poor conductivity might be one of the reasons resulting in a poor activity of NS-C-800 as compared to NS-C-900 and NS-C-1000

(Fig. 5b). The R_{CT} was calculated to be 330, 102, 29 and 58 Ω for N-C-900, NS-C-800, NS-C-900, and NS-C-1000 (Fig. S8), respectively. Notably, the N,S codoped catalysts displayed much lower R_{CT} than S-free N-C-900, suggesting that additional S doping indeed helps to accelerate the electron transfer process. The smallest R_{CT} on NS-C-900 suggests the most favorable electron transfer process when CO_2 reduction occurs on the surface of NS-C-900, contributing to the best activity.

We further estimated the electrochemical surface area (ECSA) via double-layer capacitance (C_{dl}) using cyclic voltammograms (Fig. S9) because ECSA is proportional to C_{dl}. As shown in Fig. 6c, NS-C-900 showed a C_{dl} of 17 mF cm^{-2}, which is close to that of N-C-900 (18 mF cm^{-2}) but much larger than those of NS-C-800 (8 mF cm^{-2}) and NS-C-1000 (10 mF cm^{-2}). When plotting the C_{dl} as a function of the surface area (Fig. S10), we found that they show a rough positive correlation. This observation suggests that a higher surface area is beneficial to increase the ECSA, probably because the NS-C with a larger surface area can provide more exposed effective interface between the solid carbon and liquid electrolyte. The CO partial currents were then normalized by C_{dl} (Fig. 6d) to investigate the intrinsic reason for enhanced activity on N,S-codoped carbons. It was found that NS-C-800 showed a normalized JCO of -0.082 mA cm^{-2} at -0.6 V, lower than that of NS-C-900 (-0.155 mA cm^{-2}), despite NS-C-800 had larger total N,S contents. This may be because the low heating temperature of 800 °C results in a poor conductivity and thus inhibit electron transportation. In addition, NS-C-1000 showed a smaller normalized JCO (-0.133 mA cm^{-2}) than NS-C-900, which may be as a consequence of its lower total N,S contents that decrease the numbers of catalytic sites. As for N-C-900, it presented a normalized JCO of -0.009 mA cm^{-2}, which is about 17 times smaller than that of NS-C-900. Because NS-C-900 had comparable total N contents and similar carbon architecture to N-C-900, the much better CO_2RR performance of NS-C-900 might be as a result of S modification that altered N structures and may also activate N species by modifying electronic properties.

Generally, the catalytic CO_2RR origin of N-C is considered to be from the N atoms modulation in breaking electroneutrality of carbon atoms [10,14]. This is different from the metal composite catalysts, in which the interfacial electronic properties commonly play pivotal roles in governing their catalytic activity [57]. As for N dopants, Pryi-N and Grap-N have been demonstrated to be able to create active sites for
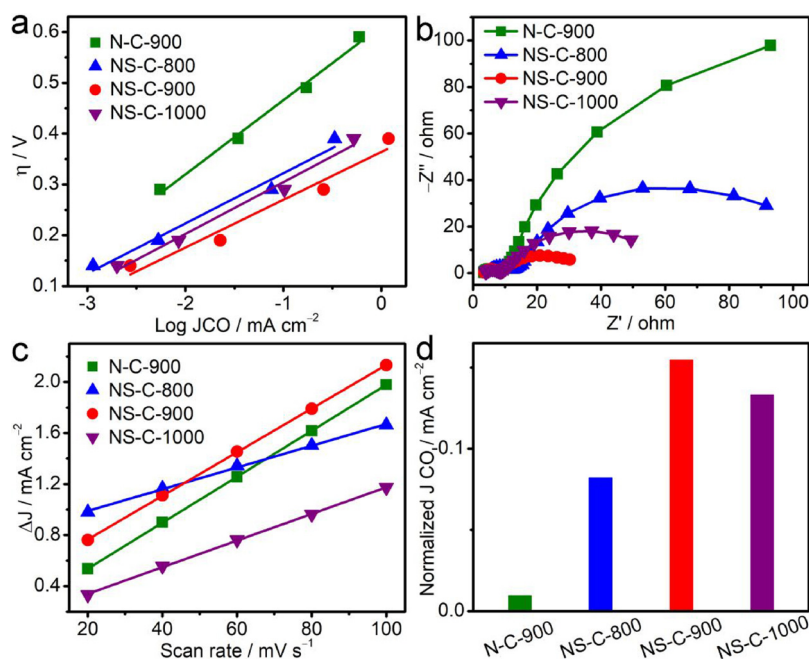
Fig. 6. (a) Tafel plots for CO production, (b) Nyquist plots at −0.6 V, (c) charging current density differences plotted against scan rates, and (d) CO partial currents at −0.6 V normalized to C_{dl} for N-C-900 and NS-C in CO_2-saturated 0.1 M $KHCO_3$ solution.

CO_2RR [5,13]. Regarding the role of S atoms, previous works have shown that S-doped carbon had a poor activity for CO_2 reduction with CO FEs below 2% [17,58]. Here, we also prepared an N-free S-doped carbon by electrochemical polymerization of ethylenedioxythiophene and then thermal carbonization at 900 °C (Fig. S11) to explore the exclusive role of S dopants toward CO_2RR. Interestingly, we found that single S-doped carbon did not yield CO but with H_2 as the sole product (Fig. S11), suggesting the inert nature of S dopants toward CO_2RR. Nevertheless, the effects of S modification on enhanced activity over NS-C cannot be ignored because our XPS analyses show that S doping significantly altered the N configurations, and NS-C possessed larger percentages of Pyri-N relative to N-C. This change may make great impacts on the observed catalytic activity since previous reports have suggested that Pyri-N and Grap-N have the different catalytic capability for CO_2RR, despite which one performs better is still controversial [5,13,14]. Furthermore, doping additional S into N-C could be able to modify the electronic properties of N-C and may thus tune their catalytic ability [23,24].

To understand whether the presence of abundant Pyri-N contributes to the enhanced activity on NS-C, DFT calculations were carried out on several Grap-N and Pyri-N moieties. Considering that Grap-N is generally located in the bulk of a carbon layer [5,59], we thus proposed that Grap-N atoms may exist in the plane (Buk_Grap-N), near edge (Edge_Grap-N), and near hole (Hole_Grap-N) of a graphitic layer (Fig. S12). As for Pyri-N, as it is located at the edge or vacancy of a graphitic layer, we constructed Pyri-N structures at edge (Edge_Pyri-N), void (Void_Pyri_N), and hole (Hole_Pyri-N) of a carbon layer (Fig. S13). Following the proposed reaction pathway from Tafel analyses and previous studies [33,56,60], we calculated the binding energy of key COOH* and CO* intermediates on various N moieties via the proton-coupled electron-transfer step. We predict that CO* has the same free energy to CO (Fig. 7a–d). This result suggests that the CO adsorption is so weak that CO can easily desorb from the catalyst surface. The weak CO adsorption could permit high CO selectivity without being further transformed into C2+ products, consistent with experimental results that CO is found to be the main product. These findings are in good agreement with reported DFT results on carbon catalysts doped by N or fluorine for CO_2 reduction [33,61], where they also found that CO cannot chemically adsorb on the catalysts surface. The similar

phenomenon has been experimentally observed on a Zn catalyst by Wang and co-workers [62]. The Zn catalyst has similar catalytic CO_2 reduction behaviors as N-doped carbon, both of which exhibit high CO selectivity. In their study, no CO adsorption band was observed by in situ spectroelectrochemical ATR-SEIRAS (surface enhanced infrared reflection absorption spectroscopy in internal attenuated total reflection configuration) method. Therefore, it is more likely that CO may directly flow into the electrolyte instead of adsorbing on the N-C and NS-C surface; however, the future in situ spectroelectrochemistry are still needed to confirm the adsorption of CO intermediate on heteroatoms-doped carbon catalysts in the CO_2 electroreduction process.

As for COOH* formation, our DFT computations reveal that the carbon atom next to graphitic N and pyridinic N atom itself are the catalytically active sites to adsorb COOH*. In addition, it was observed that the COOH* formation shows a thermodynamically uphill characteristic and thus is the potential-limiting step on all Pyri-N and Grap-N. This observation is in agreement with experimental Tafel analyses, both of which imply that CO_2 might be first transferred into COOH* and then CO. In a previous study reported by Wang and co-workers [62], the formation of COOH* intermediate has been experimentally evidenced on a Zn catalyst using in situ ATR-SEIRAS. In addition, they found that the band intensity of COOH* had a positive correlation to the CO selectivity at different potentials. This strongly suggests that the CO_2 reduction routes involves the formation of surface bonded COOH*, which is gradually consumed and further reduced to CO. Combining these together, it is inferred that CO_2 reduction may proceed on N-C and NS-C through two steps: CO_2 is firstly protonated into COOH*, then the dissociation of COOH* leads to the generation of finial gaseous CO. However, the detailed CO_2 reduction routes on heteroatoms-doped carbons are still needed to be explored in future research.

Figs. S14 and S15 present the optimized adsorption configurations of *COOH, and the free-energy diagrams are summarized in Fig. 7a and b. When the protonation of CO_2 to *COOH occurs on Grap-N, Buk_Grap-N was found to be more active than other sites, showing the lowest energy barrier of 1.22 eV. As for Pyri-N site, we observed that Void_Pyri-N had the highest catalytic capability for CO_2 activation; it exhibited the lowest Gibbs free energy of 0.30 eV for *COOH formation. Note that the energy barrier for *COOH formation on Void_Pyri-N is 0.92 eV lower as compared to that on Buk_Grap-N, predicting that Pyri-
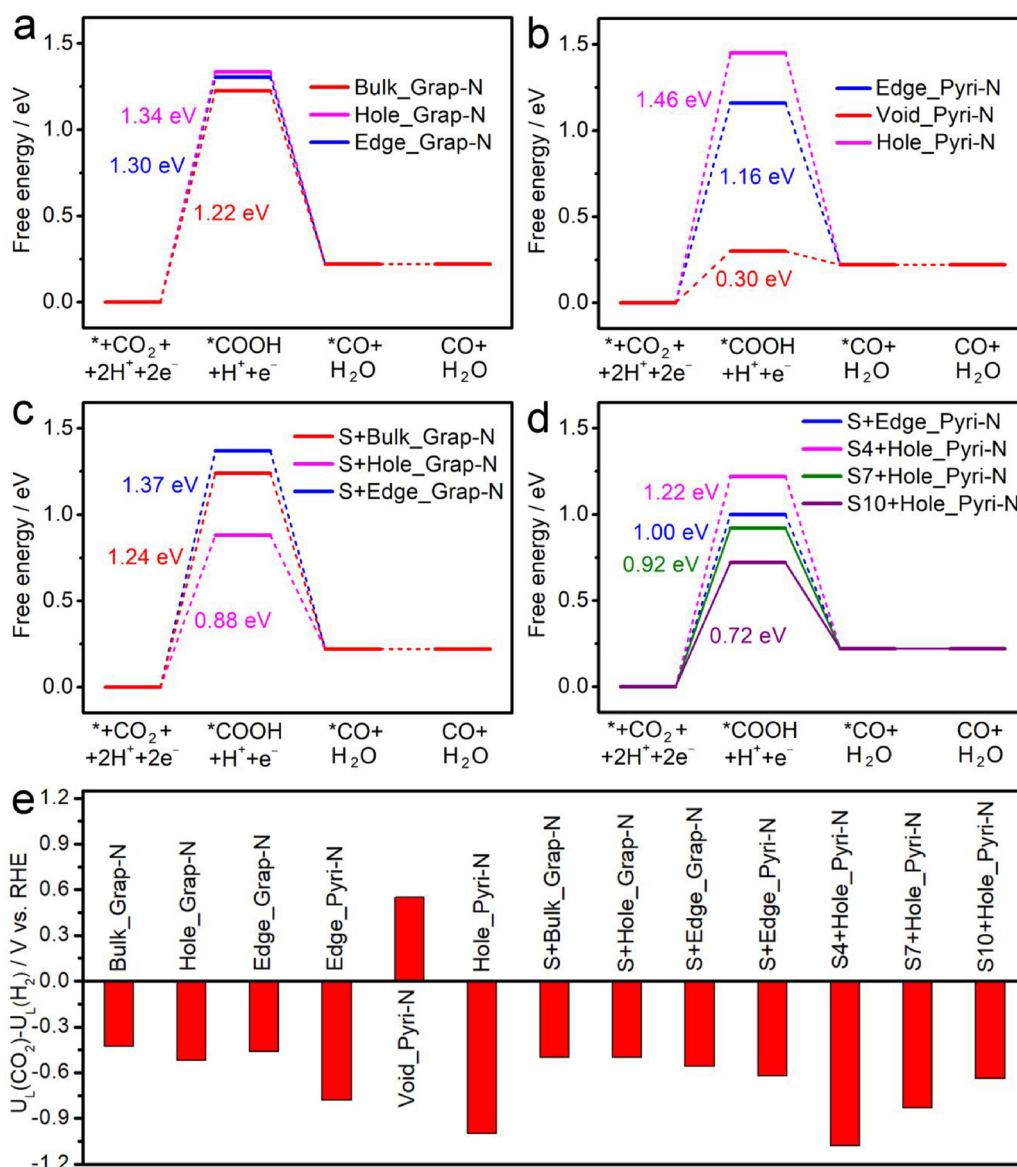
Fig. 7. Free-energy diagrams of CO_2RR at electrode potential $U = 0$ V for (a) Grap-N, (b) Pyri-N, (c) S-containing Grap-N, and (d) S-containing Pyri-N. (e) Difference in limiting potentials for CO_2 reduction and H_2 evolution on various proposed models.

N is intrinsically more active than Grap-N for catalyzing CO_2RR. This result reveals that S-induced dense Pyri-N on NS-C indeed plays a crucial role in improving CO_2 reduction activity, well explaining our experimental findings.

We further performed the DFT calculations to study the effects of S modification on the intrinsic reactivity of N dopants. As S has a much larger radius than C and N atoms, the S atom is more likely to be located at edges or holes of a carbon layer due to steric resistance effects [24,63]. Consequently, we added a S atom at the edge and hole of Grap-N and Pyri-N to generate N,S-codoped moieties (Figs. S16–S19). We observed that the incorporated S performs differently on various N dopants. Although the S addition slightly passivates Bulk_Grap-N and Edge_Grap-N by increasing the Gibbs free energy for *COOH adsorption by 0.02 eV and 0.07 eV, respectively, it significantly decreases the Gibbs free energy for *COOH adsorption by 0.46 eV on Hole_Grap-N (Fig. 7c). As for Pyri-N, it can be seen that S drastically activates both Edge_Pyri-N and Hole_Pyri-N sites (Fig. 7d). Moreover, we examined the effects of the distance between N and S atoms on the catalytic capability of Pyri-N by varying the sulfur position along the hole edge on Hole_Pyri-N. The corresponding models were named as SX + Hole_Pyri-N, where X

indicates the S position labeled in Fig. S16. It was found that the S-derived promoting contribution depends strongly on the relative distance between Pyri-N and S atoms. Upon enlarging the distance between the S atom and Pyri-N site, the catalytic capability of Pyri-N was predicted to increase, as revealed by the decreased Gibbs free energy in the order of S10 + Hole_Pyri-N (0.72 eV) < S7 + Hole_Pyri-N (0.92 eV) < S4 + Hole_Pyri-N (1.22 eV) < S-free Hole_Pyri-N (1.46 eV). This result may be related to the steric resistance induced by the larger radius of S relative to C that may weaken its electronic benefits, although the S role in enabling the improved CO_2RR process on N-C can be derived from both experiments and DFT calculations. The S-promoted activity of N dopants might be because that introducing S atoms could increase spin density of N-C [5,24,30], which has been supposed to be effective for facilitating electron transfer and adsorption of COOH* in the CO_2 reduction process [33], resulting in higher reaction rates at lower overpotentials over NS-C catalysts.

Considering that H_2 evolution is the major competitive reaction that may result in poor CO selectivity, the Gibbs free energy for HER was calculated for all the active site models (Fig. S20). Previous studies have proposed the difference between thermodynamic limiting potentials for

CO_2RR and H_2 evolution, denoted as $U_L(CO_2) − U_L(H_2)$, can act as a descriptor to gauge the selectivity for CO_2RR-generated products [64]; a larger positive $U_L(CO_2) − U_L(H_2)$ value corresponds to a higher selectivity toward CO_2 reduction. As shown in Fig. 7e, Void_Pyri-N showed the largest positive $U_L(CO_2) − U_L(H_2)$ value than other sites, suggesting its highest selectivity for CO production. Furthermore, we found that incorporating S does not impact much on the selectivity of Grap-N but significantly enhances the catalytic selectivity of Pyri-N with increased $U_L(CO_2) − U_L(H_2)$ values, consistent with the observed improved CO selectivity on NS-C with respect to N-C. Based on these computational findings with controlled experiments, it is believed that concentrated Pyri-N is the dominant catalytic site for CO_2RR on our NS-C, and S dopants are promoters that improve the catalytic reactivity and selectivity of N species for CO generation.

4. Conclusions

In summary, we developed an effective approach to boost electrocatalytic CO_2 reduction on N-doped carbons by incorporating S atoms, and the N,S-codoping synergistic effects on the activity and mechanisms toward CO_2RR were studied both experimentally and theoretically. Electrochemical measurements demonstrate that N,S-codoped carbon layers exhibited higher intrinsic activity and selectivity for CO production at lower overpotentials than the single N-doped counterpart. Both controlled experiments and theoretical DFT calculations reveal that the S atoms play two roles in promoting CO_2 reduction, facilitating the generation of abundant pyridinic N dopants as highly active CO_2RR sites and enhancing the intrinsic catalytic reactivity of both pyridinic and graphitic N by decreasing energy barrier for the formation of *COOH intermediate. With these S-induced synergistic effects, a maximum CO Faradaic efficiency of 92% was achieved at a low overpotential of 490 mV with a CO partial current of $2.63\,mA\,cm^{-2}$ on NS-C, standing out as one of the best metal-free carbon catalysts. Our study advances the understanding of synergistic electrocatalysis and thus provides a novel way to tailor electrochemical CO_2 reduction properties of doped carbons through incorporating secondary appropriate heteroatoms.

Acknowledgments

Appendix A. Supplementary data

Supplementary data associated with this article can be found, in the online version, at https://doi.org/10.1016/j.apcatb.2019.04.025.

References

[1] S. Gao, Y. Lin, X. Jiao, Y. Sun, Q. Luo, W. Zhang, D. Li, J. Yang, Y. Xie, Nature 529 (2016) 68–71.
[2] S.C. Peter, ACS Energy Lett. 3 (2018) 1557–1561.
[3] J.M. Spurgeon, B. Kumar, Energy Environ. Sci. 11 (2018) 1536–1551.
[4] O.S. Bushuyev, P. De Luna, C.T. Dinh, L. Tao, G. Saur, J. van de Lagemaat, S.O. Kelley, E.H. Sargent, Joule 2 (2018) 825–832.
[5] X. Duan, J. Xu, Z.W. Seh, J. Ma, S. Guo, S. Wang, H. Liu, S. Dou, Adv. Mater. 29 (2017) 1701784.
[6] L. Zhang, Z.-J. Zhao, J. Gong, Angew. Chem. In. Ed. 56 (2017) 11326–11353.
[7] F. Pan, A. Liang, Y. Duan, Q. Liu, J. Zhang, Y. Li, J. Mater. Chem. A 5 (2017) 13104–13111.
[8] Q. Lu, J. Rosen, Y. Zhou, G.S. Hutchings, Y.C. Kimmel, J.G. Chen, F. Jiao, Nat. Commun. 5 (2014) 3242.
[9] M. Liu, Y. Pang, B. Zhang, P. De Luna, O. Voznyy, J. Xu, X. Zheng, C.T. Dinh, F. Fan, C. Cao, F.P.G. de Arquer, T.S. Safaei, A. Mepham, A. Klinkova, E. Kumacheva, T. Filleter, D. Sinton, S.O. Kelley, E.H. Sargent, Nature 537 (2016) 382.
[10] J. Wu, R.M. Yadav, M. Liu, P.P. Sharma, C.S. Tiwary, L. Ma, X. Zou, X.-D. Zhou, B.I. Yakobson, J. Lou, P.M. Ajayan, ACS Nano 9 (2015) 5364–5371.
[11] B. Kumar, M. Asadi, D. Pisasale, S. Sinha-Ray, B.A. Rosen, R. Haasch, J. Abiade, A.L. Yarin, A. Salehi-Khojin, Nat. Commun. 4 (2013) 2819.
[12] H. Cui, Y. Guo, L. Guo, L. Wang, Z. Zhou, Z. Peng, J. Mater. Chem. A 6 (2018) 18782–18793.
[13] J. Wu, M. Liu, P.P. Sharma, R.M. Yadav, L. Ma, Y. Yang, X. Zou, X.-D. Zhou, R. Vajtai, B.I. Yakobson, J. Lou, P.M. Ajayan, Nano Lett. 16 (2016) 466–470.
[14] J. Xu, Y. Kan, R. Huang, B. Zhang, B. Wang, K.-H. Wu, Y. Lin, X. Sun, Q. Li, G. Centi, D. Su, ChemSusChem 9 (2016) 1085–1089.
[15] R. Wang, X. Sun, S. Ould-Chikh, D. Osadchii, F. Bai, F. Kapteijn, J. Gascon, ACS Appl. Mater. Interfaces 10 (2018) 14751–14758.
[16] P.P. Sharma, J. Wu, R.M. Yadav, M. Liu, C.J. Wright, C.S. Tiwary, B.I. Yakobson, J. Lou, P.M. Ajayan, X.-D. Zhou, Angew. Chem. 127 (2015) 13905–13909.
[17] W. Li, M. Seredych, E. Rodríguez-Castellón, T.J. Bandosz, ChemSusChem 9 (2016) 606–616.
[18] X. Lu, T.H. Tan, Y.H. Ng, R. Amal, Chem. Eur. J. 22 (2016) 11991–11996.
[19] X. Cui, Z. Pan, L. Zhang, H. Peng, G. Zheng, Adv. Energy Mater. 7 (2017) 1701456.
[20] W. Li, B. Herkt, M. Seredych, T.J. Bandosz, Appl. Catal. B: Environ. 207 (2017) 195–206.
[21] S. Liu, H. Yang, X. Huang, L. Liu, W. Cai, J. Gao, X. Li, T. Zhang, Y. Huang, B. Liu, Adv. Funct. Mater. 28 (2018) 1800499.
[22] J. Zhang, Z. Zhao, Z. Xia, L. Dai, Nat. Nanotechnol. 10 (2015) 444–452.
[23] D. Li, Y. Jia, G. Chang, J. Chen, H. Liu, J. Wang, Y. Hu, Y. Xia, D. Yang, X. Yao, Chem 4 (2018) 1–12.
[24] L. Ji, J. Yan, J. Mietek, Q.S. Zhang, Angew. Chem. In. Ed. 51 (2012) 11496–11500.
[25] Y. Zhao, L. Yang, S. Chen, X. Wang, Y. Ma, Q. Wu, Y. Jiang, W. Qian, Z. Hu, J. Am. Chem. Soc. 135 (2013) 1201–1204.
[26] Z. Pei, H. Li, Y. Huang, Q. Xue, Y. Huang, M. Zhu, Z. Wang, C. Zhi, Energy Environ. Sci. 10 (2017) 742–749.
[27] S. Yang, L. Zhi, K. Tang, X. Feng, J. Maier, K. Müllen, Adv. Fun. Mater. 22 (2012) 3634–3640.
[28] F. Pan, Y. Duan, A. Liang, J. Zhang, Y. Li, Electrochim. Acta 238 (2017) 375–383.
[29] D.C. Higgins, M.A. Hoque, F. Hassan, J.-Y. Choi, B. Kim, Z. Chen, ACS Catal. 4 (2014) 2734–2740.
[30] K. Qu, Y. Zheng, Y. Jiao, X. Zhang, S. Dai, S.-Z. Qiao, Adv. Energy Mater. 7 (2017) 1602068.
[31] K. Gao, B. Wang, L. Tao, B.V. Cunning, Z. Zhang, S. Wang, R.S. Ruoff, L. Qu, Adv. Mater. 0 (2019) 1805121.
[32] D. Davis, Y. Sajeev, Phys. Chem. Chem. Phys. 16 (2014) 17408–17411.
[33] J. Xie, X. Wang, J. Lv, Y. Huang, M. Wu, Y. Wang, J. Yao, Angew. Chem. In. Ed. 57 (2018) 1–6.
[34] J.K. Nørskov, J. Rossmeisl, A. Logadottir, L. Lindqvist, J.R. Kitchin, T. Bligaard, H. Jónsson, J. Phys. Chem. B 108 (2004) 17886–17892.
[35] M. Jourshabani, Z. Shariatinia, A. Badiei, Langmuir 33 (2017) 7062–7078.
[36] K. Wang, Q. Li, B. Liu, B. Cheng, W. Ho, J. Yu, Appl. Catal. B: Environ. 176 (2015) 44–52.
[37] X.-H. Li, S. Kurasch, U. Kaiser, M. Antonietti, Angew. Chem. In. Ed. 51 (2012) 9689–9692.
[38] Z. Liu, H. Nie, Z. Yang, J. Zhang, Z. Jin, Y. Lu, Z. Xiao, S. Huang, Nanoscale 5 (2013) 3283–3288.
[39] Z. Yang, Z. Yao, G. Li, G. Fang, H. Nie, Z. Liu, X. Zhou, X. Chen, S. Huang, ACS Nano 1 (2012) 205–211.
[40] F. Pan, J. Jin, X. Fu, Q. Liu, J. Zhang, ACS Appl. Mater. Interfaces 5 (2013) 11108–11114.
[41] A. Thomas, A. Fischer, F. Goettmann, M. Antonietti, J.-O. Muller, R. Schlogl, J.M. Carlsson, J. Mater. Chem. 18 (2008) 4893–4908.
[42] P. Paredez, M.E.H. Maia da Costa, L.F. Zagonel, C.T.M. Ribeiro, F. Alvarez, Carbon 45 (2007) 2678–2684.
[43] X. Wang, Y. Zhang, C. Zhi, X. Wang, D. Tang, Y. Xu, Q. Weng, X. Jiang, M. Mitome, D. Golberg, Y. Bando, Nat. Commun. 4 (2013) 2905.
[44] K. Qu, Y. Zheng, X. Zhang, K. Davey, S. Dai, S.Z. Qiao, ACS Nano 11 (2017) 7293–7300.
[45] A.C. Ferrari, D.M. Basko, Nat. Nanotechnol. 8 (2013) 235–246.
[46] J. Su, Y. Zhang, X. Zhuang, S. Li, D. Wu, F. Zhang, X. Feng, Carbon 62 (2013) 296–301.
[47] S. Yang, X. Mao, Z. Cao, Y. Yin, Z. Wang, M. Shi, H. Dong, Appl. Surf. Sci. 427 (2018) 626–634.
[48] J. Xu, G. Dong, C. Jin, M. Huang, L. Guan, ChemSusChem 6 (2013) 493–499.
[49] F. Pan, Y. Duan, X. Zhang, J. Zhang, ChemCatChem 8 (2016) 163–170.
[50] Y. Ito, W. Cong, T. Fujita, Z. Tang, M. Chen, Angew. Chem. In. Ed. 54 (2015) 2131–2136.
[51] F. Pan, W. Deng, C. Justiniano, Y. Li, Appl. Catal. B: Environ. 226 (2018) 463–472.
[52] X. Li, H. Wang, J.T. Robinson, H. Sanchez, G. Diankov, H. Dai, J. Am. Chem. Soc. 131 (2009) 15939–15944.
[53] K. Mamtani, D. Jain, D. Dogu, V. Gustin, S. Gunduz, A.C. Co, U.S. Ozkan, Appl. Catal. B: Environ. 220 (2018) 88–97.
[54] F. Pan, B. Li, X. Xiang, G. Wang, Y. Li, ACS Catal. 9 (2019) 2124–2133.
[55] T. Liu, S. Ali, Z. Lian, C. Si, D.S. Su, B. Li, J. Mater. Chem. A 6 (2018) 19998–20004.
[56] D.H. Won, H. Shin, J. Koh, J. Chung, H.S. Lee, H. Kim, S.I. Woo, Angew. Chem. In.

Ed. 55 (2016) 9297–9300.

[57] Y.-H. Wang, M.-M. Liang, Y.-J. Zhang, S. Chen, P. Radjenovic, H. Zhang, Z.-L. Yang, X.-S. Zhou, Z.-Q. Tian, J.-F. Li, Angew. Chem. 130 (2018) 11427–11431.

[58] W. Li, T.J. Bandosz, ChemSusChem 11 (2018) 2987–2999.

[59] D. Guo, R. Shibuya, C. Akiba, S. Saji, T. Kondo, J. Nakamura, Science 351 (2016) 361–365.

[60] F. Pan, H. Zhang, K. Liu, D.A. Cullen, K.L. More, M. Wang, Z. Feng, G. Wang, G. Wu, Y. Li, ACS Catal. 8 (2018) 3116–3122.

[61] R. Daiyan, X. Tan, R. Chen, W.H. Saputera, H.A. Tahini, E.C. Lovell, Y.H. Ng, S.C. Smith, L. Dai, X. Lu, R. Amal, ACS Energy Lett. 3 (2018) 2292–2298.

[62] K. Jiang, H. Wang, W.-B. Cai, H. Wang, ACS Nano 11 (2017) 6451–6458.

[63] H.B. Yang, J. Miao, S.-F. Hung, J. Chen, H.B. Tao, X. Wang, L. Zhang, R. Chen, J. Gao, H.M. Chen, L. Dai, B. Liu, Sci. Adv. 2 (2016) e1501122.

[64] W. Bi, X. Li, R. You, M. Chen, R. Yuan, W. Huang, X. Wu, W. Chu, C. Wu, Y. Xie, Adv. Mater. (2018) 1706617.